



Synergic grain boundary segregation and precipitation in W- and W-Mo-containing high-entropy borides

Chunyang Wang^a, Mingde Qin^b, Tianjiao Lei^c, Yubin He^a, Kim Kisslinger^e,
Timothy J. Rupert^{c,d}, Jian Luo^b, Huolin L. Xin^{a,*}

^a Department of Physics and Astronomy, University of California, Irvine, CA, 92697, USA

^b Department of NanoEngineering, Program of Materials Science and Engineering, University of California, San Diego, La Jolla, CA, 92093, USA

^c Department of Materials Science and Engineering, University of California, Irvine, CA, 92697, USA

^d Department of Mechanical and Aerospace Engineering, University of California, Irvine, CA, 92697, USA

^e Center for Functional Nanomaterials, Brookhaven National Laboratory, Upton, NY, 11973, USA

ARTICLE INFO

Keywords:

High-entropy ceramics
High-entropy borides
Grain boundary
Segregation
Precipitation

ABSTRACT

The structures of W- and W-Mo-containing high-entropy borides (HEBs) are systematically studied by combining atomic-resolution transmission electron microscopy imaging, electron diffraction, and chemical analysis. We reveal that W or W-Mo addition in HEBs leads to segregation of these elements to the grain boundaries (GBs). In the meantime, W- or W-Mo-rich precipitates also form along the GBs. Crystallographic analysis and atomic-scale imaging show that the GB precipitates in both W- and W-Mo-containing HEBs have a cube-on-cube orientation relationship with the matrix. With further strain analysis, the coherency of the precipitate/matrix interface is validated. Nanoindentation tests show that the simultaneous GB segregation and coherent precipitation, as a supplement to the grain hardening, provide additional hardening of the HEBs. Our work provides an in-depth understanding of the GB segregation and precipitation behaviors of HEBs. It suggests that GB engineering could be potentially used for optimizing the performance of high-entropy ceramics.

1. Introduction

High-entropy alloys (HEAs), since the stimulating reports by Cantor et al. [1] and Yeh et al. [2,3] in 2004, have generated extensive interest in the metallurgy community. Since then, high-entropy ceramics have also been widely explored. For example, Rost et al. [4] reported an entropy-stabilized bulk oxide, $(\text{Mg}_{0.2}\text{Zn}_{0.2}\text{Co}_{0.2}\text{Cu}_{0.2}\text{Zn}_{0.2})\text{O}$, as the ceramic counterpart to HEAs. Later on, entropy-stabilized ceramics rapidly expanded from oxides [5–7] to borides [8–11], carbides [12] nitrides [13–16] and silicides [17,18]. In particular, several classes of high-entropy borides (HEBs) have been successfully fabricated [8,10,11,19]. Specifically, Gild et al. first fabricated high-entropy metal diborides with the AlB_2 -prototype structure as the first HEBs and a new class of high-entropy ultra-high temperature ceramics (UHTCs) [8]. These HEBs, which represent the first non-oxide bulk high-entropy ceramics, show improved hardness and oxidation resistance than the average performance of individual metal diborides. Later, this approach was extended to other HEBs such as W- and W-Mo-containing HEBs, but single-phase HEBs were not obtained [20]. Different from the conventional reactive

spark plasma sintering (SPS) of a mixture of binary diborides, Tallarita et al. [21,22] tried direct fabrication of $(\text{Ti}_{0.2}\text{Zr}_{0.2}\text{Hf}_{0.2}\text{Nb}_{0.2}\text{Mo}_{0.2})\text{B}_2$ by reactive SPS of elemental boron and metals in one step (1950 °C, 20 min, 20 MPa), but did not achieve a high density or uniform microstructure due to out-gassing. Qin et al. [20] extended reactive SPS of elemental boron and metals to fabricate W and W-Mo-containing HEBs. In contrast to conventional reactive SPS of mixtures of metal diborides which leads to multi-phase HEBs, this approach successfully produced single-phase polycrystalline HEBs. More importantly, they found that the W- and W-Mo-containing HEBs are significantly harder than $(\text{Ti}_{0.2}\text{Zr}_{0.2}\text{Hf}_{0.2}\text{Nb}_{0.2}\text{Ta}_{0.2})\text{B}_2$ derived from harder binary boride components. This interesting finding implies that high-entropy ceramics could potentially achieve unexpected properties beyond the simple mixture effect and therefore may have important applications in designing new generation UHTCs. However, based on the above results, the origin of the hardening effects in W- and W-Mo-containing HEBs remains unknown and an in-depth understanding of the atomic structure and the structure-mechanical property relationship of the HEBs is still lacking. In this study, by combining atomic-resolution transmission

* Corresponding author at: 4129 Frederick Reines Hall, Irvine, CA, 92697-4575, USA.

E-mail address: huolinx@uci.edu (H.L. Xin).

<https://doi.org/10.1016/j.jeurceramsoc.2021.04.004>

Received 2 February 2021; Received in revised form 31 March 2021; Accepted 2 April 2021

Available online 7 April 2021

0955-2219/© 2021 Elsevier Ltd. All rights reserved.

Table 1
Nominal composition and hardness of HEB-A1, HEB-E1, and HEB-F1 from Ref. [20].

	HEB-A1	HEB-E1	HEB-F1
Composition	$(\text{Ti}_{0.2}\text{Zr}_{0.2}\text{Hf}_{0.2}\text{Nb}_{0.2}\text{Ta}_{0.2})\text{B}_2$	$(\text{Zr}_{0.2}\text{Hf}_{0.2}\text{Nb}_{0.2}\text{Ta}_{0.2}\text{W}_{0.2})\text{B}_2$	$(\text{Zr}_{0.225}\text{Hf}_{0.225}\text{Nb}_{0.225}\text{Mo}_{0.225}\text{W}_{0.1})\text{B}_2$
Hardness	20.9 GPa	26.7 GPa	27.5 GPa

electron microscopy (TEM) imaging, electron diffraction, and chemical analysis, we perform a comparative study on three similar single-phase HEBs with different compositions fabricated by reactive SPS of elemental boron and metals. The influence of W and W-Mo additions on the structures of the HEBs are studied. Especially, the grain boundary segregation and precipitation behaviors are systematically investigated. Nanoindentation experiments are performed to understand the influence of the GB segregation and precipitation on the hardening of the HEBs.

2. Materials and methods

HEBs were synthesized via reactive sintering of elemental boron and metals [20]. For boron-metals reactive SPS, elemental powders of Hf, Ta, Ti, Zr, Nb, Mo, and W (> 99 % purity, purchased from Alfa Aesar, MA, USA) and boron (99 % purity, 1 – 2 μm , purchased from US Research Nanomaterials, TX, USA) were used to fabricate three specimens with the similar single-phase structure (AlB_2 -structured, space group $\text{P6}/\text{mmm}$) but different compositions [20], namely HEB-A1, HEB-E1 and HEB-F1 listed in Table 1. The compositions of HEB-A1, HEB-E1 and HEB-F1 are $(\text{Ti}_{0.2}\text{Zr}_{0.2}\text{Hf}_{0.2}\text{Nb}_{0.2}\text{Ta}_{0.2})\text{B}_2$, $(\text{Zr}_{0.2}\text{Hf}_{0.2}\text{Nb}_{0.2}\text{Ta}_{0.2}\text{W}_{0.2})\text{B}_2$ and $(\text{Zr}_{0.225}\text{Hf}_{0.225}\text{Nb}_{0.225}\text{Mo}_{0.225}\text{W}_{0.1})\text{B}_2$, respectively. The powders were hand-mixed and subsequently processed by high-energy ball milling (HEBM) in a Spex 8000D mill (SpexCertPrep, NJ, USA) in tungsten carbide lined stainless steel jars and 10 mm

tungsten carbide milling media (ball-to-powder ratio $\approx 4:1$), for 50 min with 1 wt. % (0.05 g) stearic acid as a lubricant. The HEBM was performed in an argon atmosphere (O_2 content below 10 ppm). The milled powders were loaded into 10 mm graphite dies and then consolidated into dense pellets via SPS in vacuum (10^{-2} Torr) using a Thermal Technologies 3000 series SPS (CA, USA). During the initial temperature ramping (50 $^\circ\text{C}/\text{min}$), a uniaxial load of 10 MPa was applied to facilitate the reaction. The specimen was first held in SPS at 1400 $^\circ\text{C}$ and 1600 $^\circ\text{C}$, for 40 min each, to allow out-gassing and reduction of native oxides with excess boron. The temperature was then raised to 2000 $^\circ\text{C}$ at a heating rate of 30 $^\circ\text{C}/\text{min}$. After that, the specimen was sintered isothermally for 10 min for final densification, meanwhile, the uniaxial load was increased to 50 MPa at a rate of 5 MPa/min. Finally, the sintered specimens were cooled to room temperature in the SPS machine.

Vickers microhardness tests were carried out on a diamond indenter (indenter size of approximately 10–13 μm) with a loading force of 1.96 N (200 gf) and a holding time of 15 s according to ASTM C1327. Over 50 measurements were conducted at different locations to ensure statistical validity. The hardness of HEB-A1, HEB-E1, and HEB-F1 is determined as 20.9 GPa, 26.7 GPa, and 27.5 GPa, respectively, as listed in Table 1.

To prepare TEM samples, sintered specimens were first ground (to remove carbon contamination from graphite tooling) and then polished. After that, focused-ion beam (FIB) milling (FEI's dual-beam SEM/FIB system) was used to prepare TEM samples containing multiple grain boundaries. The samples prepared by FIB were further thinned to

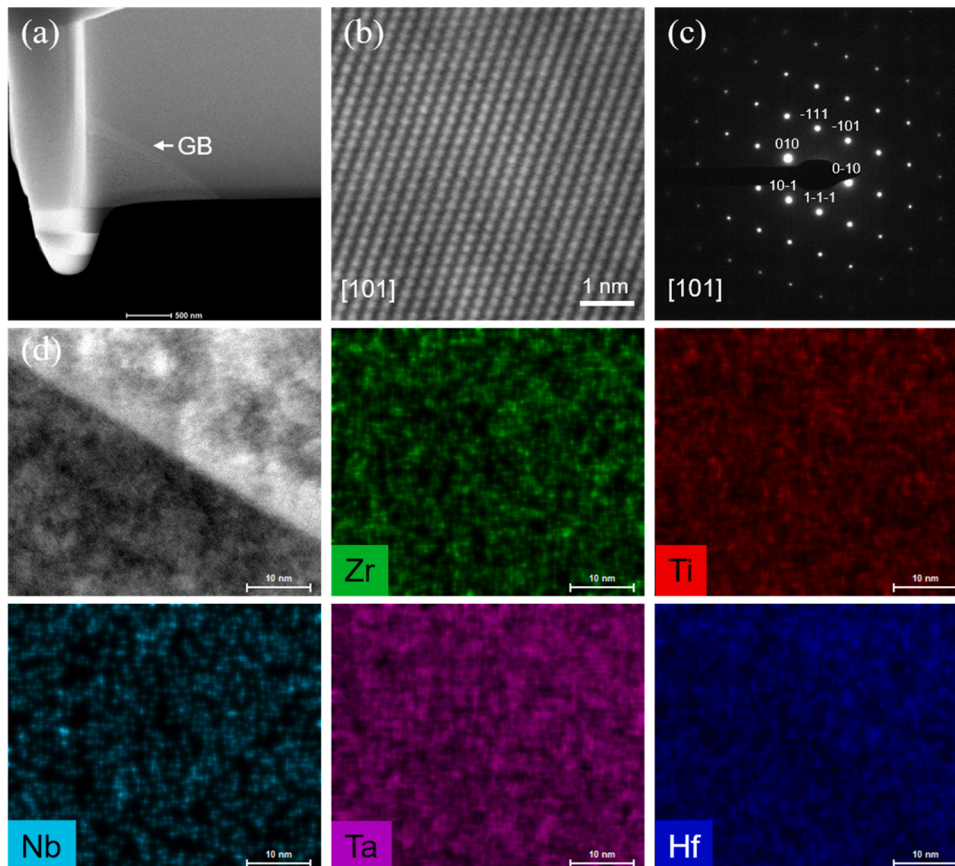


Fig. 1. Structure and chemistry of $(\text{Ti}_{0.2}\text{Zr}_{0.2}\text{Hf}_{0.2}\text{Nb}_{0.2}\text{Ta}_{0.2})\text{B}_2$ (HEB-A1). (a) A high-angle annular dark-field scanning transmission electron microscopy (HAADF-STEM) image of the HEB-A1 specimen. (b) An atomic-resolution HAADF-STEM image of the HEB-A1 taken along the [101] zone axis. (c) Electron diffraction pattern (EDP) of the grain corresponding to that in (b). (d) Representative high spatial-resolution energy dispersive spectroscopy (EDS) maps of Zr, Ti, Nb, Ta, and Hf across an edge-on grain boundary (GB) in the HEB-A1 specimen.

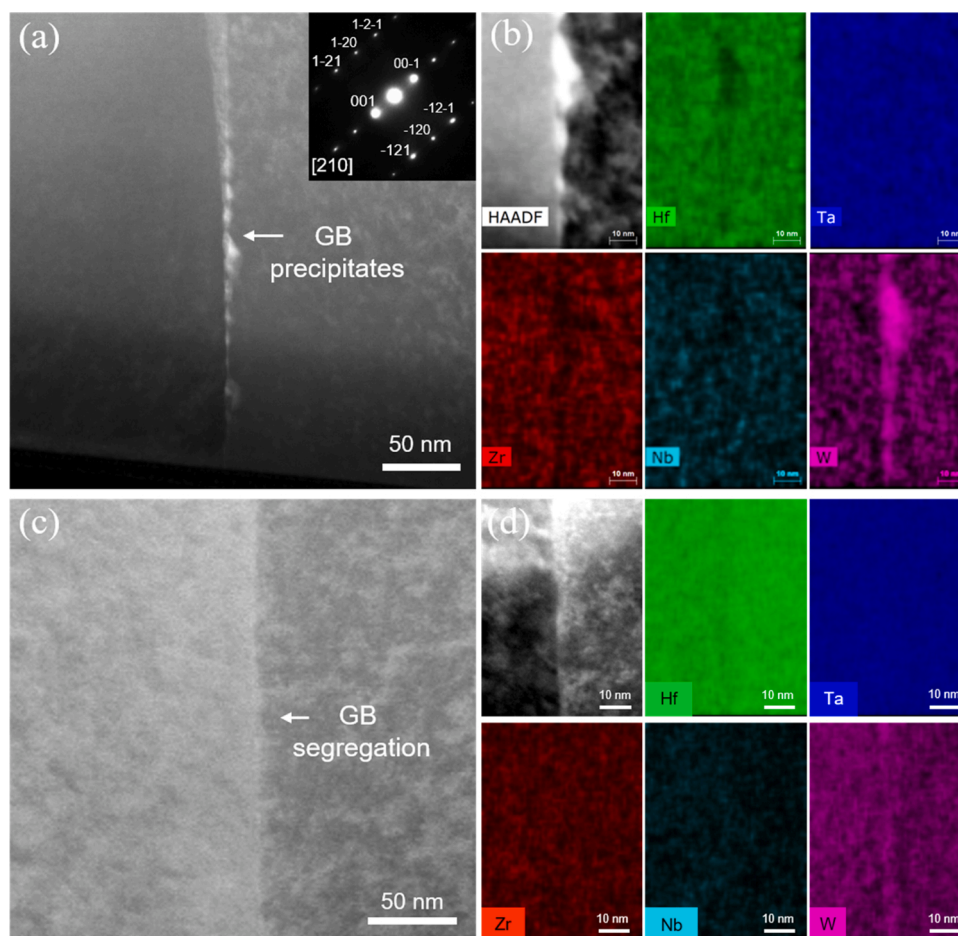


Fig. 2. Grain boundary segregation and precipitation in the HEB-E1. (a) A HAADF-STEM image of a GB in the HEB-E1. GB precipitates (regions with brighter contrast) are indicated by the arrow. The inset shows the EDP of the HEB-E1 taken along the [210] zone axis. (b) EDS maps of Hf, Ta, Zr, Nb, and W across the GB in (a). (c) A HAADF-STEM image of another GB region without precipitates. (d) EDS maps of Hf, Ta, Zr, Nb, and W across the GB in (c). W segregation is identified at the GB.

electron transparent by using ion milling (Fischione Model 1040 NanoMill). The (S)TEM imaging and chemical analysis were carried out on a (scanning) transmission electron microscope with a field emission source operated at 200 KeV. Atomic-resolution imaging was performed in high-angle annular dark-field scanning transmission electron microscopy (HAADF-STEM) mode. Energy-dispersive X-ray spectroscopy (EDS) elemental mapping was performed in HAADF-STEM mode with a multi-head EDS system integrated into the TEM.

3. Results and discussions

Fig. 1 shows TEM characterization of the structure and chemistry of the baseline HEB-A1 specimen. The atomic-resolution HAADF-STEM image (Fig. 1(b)) as well as electron diffraction pattern (EDP) (Fig. 1(c)) taken along the [101] zone axis shows that HEB-A1 has a perfect AlB_2 structure (space group, $P6/mmm$). Importantly, it is worth noting that except for the Bragg spots corresponding to a perfect AlB_2 structure, no other frequencies are observed in the EDP, suggesting that the short-range ordering (SRO) widely existing in some of the high-entropy alloys [23] are not observed in HEB-A1. Furthermore, the chemistry of the GBs of HEB-A1 was statistically investigated. For example, Fig. 1(d) shows high-resolution EDS maps of a GB on edge-on condition. The result shows that the distributions of all the constituent elements are homogeneous across the GB, indicating that Zr, Ti, Nb, Ta, and Hf incline to distribute uniformly in the sample with no obvious tendency to segregate to the GBs.

By replacing the Ti in HEB-E1 with W, another single-phase HEB specimen, i.e., $(Zr_{0.2}Hf_{0.2}Nb_{0.2}Ta_{0.2}W_{0.2})B_2$ (HEB-E1) was also fabricated by boron-metal reactive SPS. The structure and chemistry of the HEB-E1 were comprehensively studied by TEM. Fig. 2(a) shows a representative GB region with substantial precipitates formed along the GB. It is worth noting that, similar to the baseline HEB-A1, SRO is also not obviously observed in the sample from the EDP (inset of Fig. 2(a)). EDS maps (Fig. 2(b)) show that the precipitates are rich in W. Detailed EDS quantification (Tables S1) shows that the precipitates are mainly composed of W (77.9 at.%), with a small amount of Ta (12.7 at.%) and Nb (7.2 at.%), and barely contain Hf and Zr. That is to say, the addition of W enables the formation of W-rich precipitates, rather than single element diborides such as WB_2 . Aside from the GB regions with precipitates, GB regions without precipitates were also studied and the chemical state of these regions was statistically investigated. For instance, Fig. 2(c) shows a representative HAADF-STEM image of a GB region without precipitates. High-resolution EDS maps (Fig. 2(d)) across the GB show evident segregation of W to the GB plane. To sum up, the above results indicate that compared with the elements (Zr, Ti, Nb, Ta, and Hf) in the baseline HEB-A1 specimen, W has a high tendency to segregate to GBs, and once the segregation exceeds the solubility, W-rich phases start to precipitate along the GB.

Detailed characterization was performed to determine the structure of the precipitates by combining electron diffraction and atomic imaging. Fig. 3(a) shows an experimental EDP of the interface between the matrix and precipitate. Two sets of Bragg spots both correspond to AlB_2 -

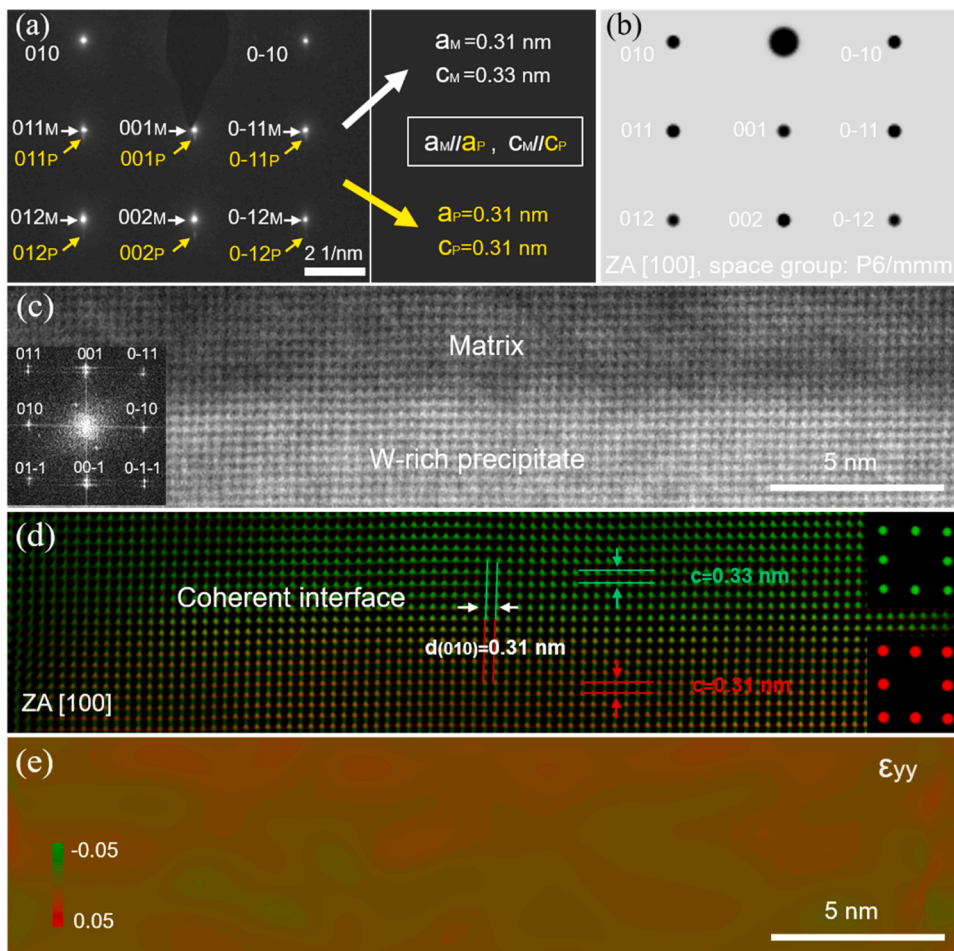


Fig. 3. Atomic structure of the matrix/precipitate interface in HEB-E1. (a) A representative EDP of the matrix/precipitate interface. Two sets of Bragg spots corresponding to the matrix and precipitate are indicated by white and yellow arrows, respectively. Lattice parameters of the matrix and precipitate were determined based on the EDPs. (b) A simulated EDP of AlB_2 structure. (c) Atomic-resolution HAADF-STEM image of a matrix/precipitate interface. The left inset shows the Fast Fourier Transform (FFT) of the interface in which two sets of Bragg spots are identified. (d) Filtered and false-colored image of the interface through overlapping the inverted FFT of the two sets of Bragg spots. Insets show the selected Bragg spots corresponding to the matrix (green) and the precipitate (red), respectively. (e) Strain map obtained by geometrical phase analysis (GPA). The result shows negligible strain at the interface along the c axis, indicating the interface is nearly coherent. (For interpretation of the references to colour in the Figure, the reader is referred to the web version of this article).

type structure (space group: $P6/mmm$) were identified. Fig. 3(b) shows a simulated EDP of the matrix along the $[100]$ zone axis. Based on the EDP, the lattice parameters of both the matrix ($a_m = b_m = 0.310$ nm, $c_m = 0.333$ nm) and precipitate ($a_p = b_p = 0.310$ nm, $c_p = 0.309$ nm) are determined. Fig. 3(c) shows a representative atomic-resolution HAADF-STEM image of the matrix/precipitate interface (See HRTEM image of a similar interface obtained from another zone axis in Fig. S1). Similarly, two sets of Bragg spots (inset in Fig. 3(c)) were identified as that shown in Fig. 3(b). Fig. 3(d) highlights the atomic structure of the interface through inverse Fast Fourier Transform (FFT) of the two sets of Bragg spots. Measurements based on the FFT and diffraction pattern show that the c axis of the precipitate is slightly smaller than that of the matrix, while the misfit between the (010) planes is too small to be identified from the overlapped Bragg spots in the EDP. To evaluate the misfit, lattice parameters of both the matrix and precipitate were calculated by Vegard's law based on their compositions (Table S2). The calculated lattice parameters are basically in good agreement with those derived from our experiments. According to the calculated parameters, the misfit between the a axes of the matrix and precipitate is as small as 1.6 %, which explains the overlapped (010) planes shown in the EDP and FFT in Figs. 3(b) and (c) and thereby rationalizes the nearly coherent interface between the precipitate and the matrix. The coherency of the interface was also validated by strain analysis obtained by geometrical phase analysis (Fig. 3 e), whereby negligible strain was identified. A similar nearly coherent interface was also observed at GBs (see an example in Fig. S2). It is worth noting that, aside from GB precipitates which are dominant in the sample, a small number of precipitates are also observed in the grain interior (Fig. S3). Occasionally, a few precipitates with larger size (size below 100 nm) with lath or irregular

shape were also observed in local GB regions of the HEB-E1 specimen.

Furthermore, we fabricated HEB-F1 by replacing the Ti and Zr in baseline HEB-A1 with W and Mo. Fig. 4(a) shows a low magnification HAADF-STEM image of an HEB-F1 sample containing three GBs. Similar to that in baseline HEB-A1, no obvious SRO was identified based on both atomic-resolution imaging and electron diffraction (Fig. S4). Periodical lath-shaped nano-precipitates were observed to form along the GBs (see an enlarged image corresponding to the boxed region in Fig. 4(a)). Note that although the precipitates at the lower two GBs in Fig. 4(a) are hardly visible due to the blocking by the matrix, they are observed after tilting the sample in TEM. Aside from that, a precipitate was observed to form in the triple junction of the three GBs. EDS maps of the GB (Fig. 4 (b)) show that the precipitates are rich in W and Mo. Fig. 4(c) shows an atomic-resolution HAADF-STEM image of a representative lath-shaped precipitate at the GB. Fig. 4(d) shows a filtered image (the matrix and precipitates are highlighted by green and red, respectively) corresponding to the boxed region in Fig. 4(c). The two sets of Bragg spots (inset in Fig. 4(d)) show that the $[100]$ zone axis of the precipitate is parallel to that of the matrix and no misfit dislocations are formed at the interface. Similar to the matrix/precipitate interface in HEB-E1, the c axis of the W-Mo-rich precipitate is slightly smaller than that of the matrix, while the misfit between the (010) planes are too small to be identified from the overlapped Bragg spots in the EDP, indicating the a axes of the matrix and precipitate are nearly coherent. The coherency of the interface was also validated by strain analysis obtained by geometrical phase analysis (Fig. 4 e), whereby negligible strain was identified.

Moreover, the structure and chemistry of GB regions in HEB-F1 without precipitates were also investigated. Fig. 5(a) shows a representative atomic-resolution HAADF-STEM image of a GB region with no

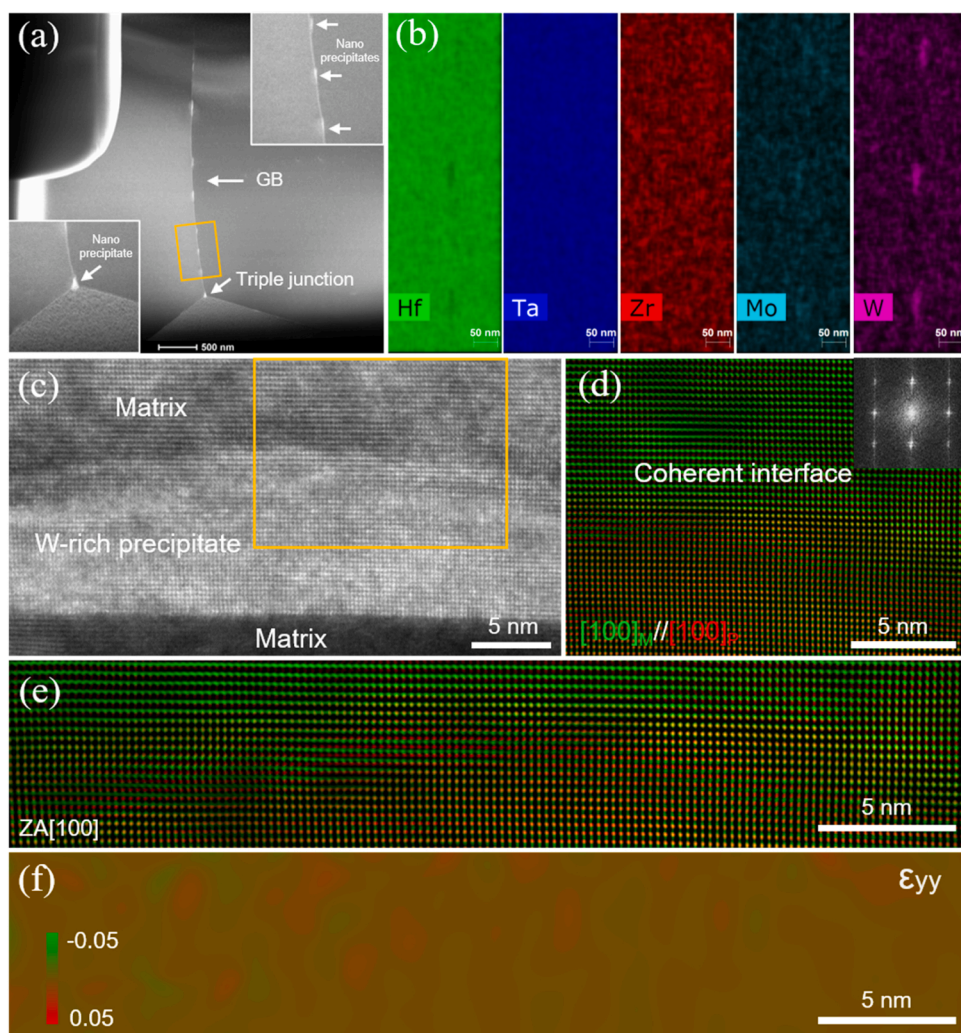


Fig. 4. W-Mo-rich GB precipitation and atomic structure of matrix/precipitate interface at the GB of HEB-F1. (a) Low magnification HAADF-STEM image of an HEB-F1 TEM sample containing three GBs. The upper right inset shows an enlarged image of the boxed region. Periodical nano precipitates (indicated by the arrows) are identified at the GB. The lower left inset highlights a nano precipitate pinning at a GB triple junction. (b) EDS maps of Hf, Ta, Zr, Mo, and W across the GB in (a). Enrichment of Mo and W are identified. (c) Atomic-resolution HAADF-STEM image of the matrix/precipitate interface taken along [001] zone axis. (d) FFT-filtered image of the boxed region in (c). The matrix and precipitate are highlighted by green and red, respectively. Inset shows the FFT of the interface where two sets of Bragg spots corresponding to the matrix and precipitate are identified. (e,f) Strain analysis by GPA. The result shows negligible strain at the interface along the c axis, indicating the matrix/precipitate interface is nearly coherent. (For interpretation of the references to colour in the Figure, the reader is referred to the web version of this article).

precipitates. Periodically atomic features (indicated by the arrows in Fig. 5(a)) with brighter contrast were directly observed at the GB. Since the contrast of the HAADF-STEM image is proportional to atomic numbers (HAADF-STEM image is formed by incoherent imaging with high angle scattered electrons), it suggests that heavier atoms possibly segregated to the GB. To confirm that, high-resolution EDS maps (Fig. 5 (b)) were performed. The results show that W and Mo simultaneously segregated to the GB.

According to the microhardness results shown in Table 1, HEB-E1 and HEB-F1 have evidently enhanced hardness compared with the baseline HEB-A1. To explore the influence of the concurrent GB segregation and precipitates on the hardening of the HEBs, statistical nanoindentation tests were performed on both grain interior and regions containing GBs (Fig. S5). The results summarized in Table 2 show that compared with the baseline HEB-A1, the hardness of HEB-E1 and HEB-F1 grains increases by approximately 5 GPa and 6 GPa, respectively, indicating an evident grain hardening effect arising from the grain interior. Furthermore, due to the introduction of GB segregation and precipitation, the hardness of the GB regions is increased by approximately 2 GPa, indicating that the GB hardening effect due to the concurrent GB segregation and precipitation lead to extra hardening of the HEBs. It is worth noting that due to the small volume fraction of each GB under the nanoindenter, the hardness of the GBs is likely underestimated. Despite that, due to the limited total volume fraction of the GBs in the HEBs, the GB hardening effect is not likely the dominant factor that contributes to the hardening of the W- or W-Mo-containing

HEBs. Yet it is reasonable to speculate that if the grain size of HEB-F1 is reduced to that comparable to the grain size of HEB-E1, the hardness of HEB-F1 could be considerably enhanced by the increased contribution from the GBs. The deep insights gained from the GB structures and performance suggest that the synergy of GB segregation and coherent precipitation could be potentially used to dramatically improve the mechanical performance of HEBs when their grain sizes are reduced to submicron- or even nano-size regime.

The grain size distribution directly determines the volume fraction of the GBs in the three types of HEBs. Therefore, its potential influence on the hardening of the materials needs to be taken into consideration. According to our previous results [20], the averaged grain sizes of HEB-A1, HEB-E1, and HEB-F1 are 12.7 μm , 14.8 μm , and 20.7 μm , respectively. That is, the grain sizes of HEB-A1 and HEB-E1 are similar, while the grain size of HEB-F1 is evidently larger. Due to the increased averaged grain size, the total volume fraction of GBs in HEB-F1 should be readily reduced and, in that way, the contribution of the GB hardening to the overall hardness improvement of HEB-F1 is supposed to be less significant than that in HEB-E1. This is in good agreement with the hardness tests in both Tables 1 and 2 which show relatively small hardness improvement for HEB-F1 compared with HEB-E1. It is reasonable to speculate that if the grain size of HEB-F1 is reduced to that comparable to HEB-E1, the hardness of HEB-F1 could be considerably enhanced by the increased contribution from the GBs. Besides, it is noteworthy that although the total volume ratio of the GBs and the density of the GB precipitates in HEB-F1 are lower than that in HEB-E1,

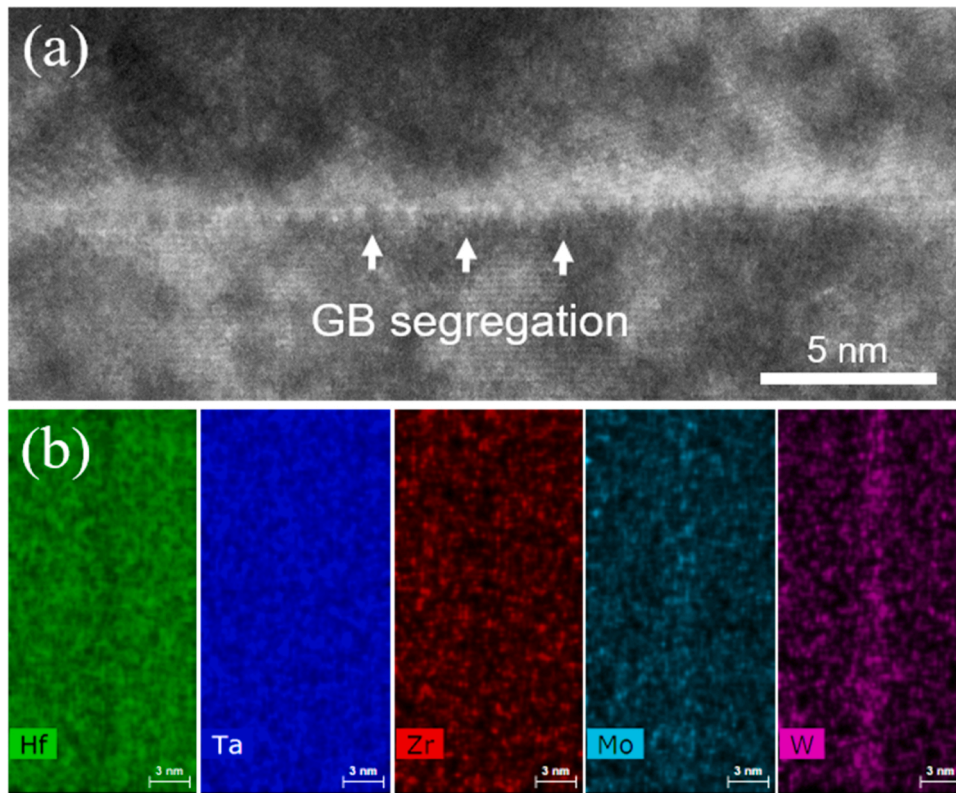


Fig. 5. W-Mo co-segregation to the GBs in the HEB-F1. (a) Atomic-resolution HAADF-STEM image of a GB. (b) EDS maps of the compositions across the GB in (a). Simultaneous segregation of W and Mo is identified.

Table 2

Nanoindentation hardness test results for grain interior regions and regions containing GBs of HEB-A1, HEB-E1, and HEB-F1, respectively. The indenter size is around 4–6 μm . The loading force is 500 mN. Over 20 measurements were conducted at different locations for each sample to ensure statistical validity.

	HEB-A1 grain	HEB-A1 GB	HEB-E1 grain	HEB-E1 GB	HEB-F1 grain	HEB-F1 GB
Hardness	25.9 GPa	26.6 GPa	30.5 GPa	32.3 GPa	32.1 GPa	34.2 GPa

the GB hardness of HEB-F1 still increases by about 2 GPa compared with that of HEB-E1. This confirms the advantage of dual-element (W-Mo) co-segregation and W-Mo-rich precipitation over single-element (W) segregation and precipitation.

High-temperature intergranular fracture is a widely observed failure mode in UHTCs [24–27]. For instance, Kalish et al. [24] and Bird et al. [25] reported that the grains of HfB_2 and ZrB_2 craze by intergranular fracture at 1400 °C. Therefore, GB strengthening or hardening plays an important role in enhancing the high-temperature mechanical properties of UHTCs. GB segregation and precipitation which widely exist in alloys [28–30] or ceramics [31–33] could have an important impact on the high-temperature mechanical properties of the materials. For example, Dai et al. [32] performed systematic first-principles investigations on the segregations of a series of solute atoms including Y, Nb, Ta, Mo, and W in the GBs of ZrB_2 . They suggested that the short equilibrium M–B bonds (M=Nb, Ta, Mo, or W) induce local contractions around GBs and thereby enhance the mechanical properties of ZrB_2 at elevated temperatures. From the experimental side, Ma et al. [33] reported segregation of W at the GBs of ZrB_2 in strong ZrB_2 -SiC-WC ceramics. The W segregation and its interaction with high-density dislocations are considered to contribute to the excellent high-temperature mechanical properties of ZrB_2 -SiC-WC ceramics. Based on the above

findings, it can be conjectured that the W segregation and W-Mo co-segregation observed in this work are likely to contribute to the high-temperature performances of the HEBs. As for the precipitates, precipitation strengthening has been widely demonstrated to improve the high-temperature performance of HEAs, e.g., high-entropy refractory alloys [34]. In particular, coherent precipitation strengthening has been demonstrated as an effective way to improve the high-temperature performances of HEAs. For instance, $\text{AlMo}_{0.5}\text{Nb-Ta}_{0.5}\text{TiZr}$ which has a B2/BCC coherent nanophase structure shows high-temperature specific strength that is much superior to Ni-based superalloys. [35] Therefore, we believe, due to the nearly perfect cube-on-cube crystallographic orientation of the precipitation/matrix interface, the high-temperature mechanical performances of the W- and W-Mo-containing HEBs could be benefited. This is because the coherency of the precipitate-matrix interface could effectively mitigate the stress-concentration-induced intergranular cracking at high temperature.

GB engineering is an important and widely adopted strategy for tailoring the mechanical properties of both metallic materials [36,37] and ceramics [32,33]. In particular, the high-entropy GB effect [38] is a novel strategy recently proposed to stabilize nanocrystalline alloys at high temperatures. For example, by introducing one or more GB segregation elements, a high-entropy GB effect could be achieved and coupled with bulk high-entropy effects to enhance the performance of nanocrystalline alloys [39]. In this work, we demonstrate that with the increase of the segregation species, e.g., W-Mo co-segregation in HEB-F1 specimen, the hardness of the borides could be further improved compared with single-element segregation (e.g., W segregation in HEB-E1 specimen). This could be possibly explained by the fact that multicomponent segregation at GBs may maximize the solute-drag effects [40,41]. It is speculated that the introduction of multi-component segregation (more than two components) to GBs may further harden the HEBs. Moreover, by adjusting the content of the components which are

prone to segregate to GBs, the degree and contribution of GB segregation and precipitation to the overall GB hardening effects could be well controlled to reach an optimal performance of HEBs in the future.

4. Conclusions

In conclusion, by combining atomic-resolution TEM imaging, electron diffraction, and chemical analysis, we systematically investigate the atomic structure and chemistry of W- and W-Mo-containing HEBs. Concurrent GB segregation (or co-segregation) and precipitation are uncovered in both the W- and W-Mo-containing HEBs. The segregation and coherent precipitation lead to extra hardening of both HEBs. Our work demonstrates the effectiveness of hardening high-entropy ceramics through the synergy of GB segregation and precipitation. We anticipate that the new insights gained from this work will provide important guidance for the fabrication of super-hard nanocrystalline HEBs or other ceramics through GB engineering.

Declaration of Competing Interest

The authors declare that they have no known competing financial interests or personal relationships that could have appeared to influence the work reported in this paper.

Acknowledgements

This research was primarily supported by the National Science Foundation Materials Research Science and Engineering Center program through the UC Irvine Center for Complex and Active Materials (DMR-2011967). The authors acknowledge the use of facilities and instrumentation at the UC Irvine Materials Research Institute (IMRI), which is supported in part by the National Science Foundation through the UC Irvine Materials Research Science and Engineering Center (DMR-2011967). This research used resources of the Center for Functional Nanomaterials (CFN), which is a U.S. Department of Energy Office of Science User Facility, at Brookhaven National Laboratory under Contract No. DE-SC0012704.

Appendix A. Supplementary data

Supplementary material related to this article can be found, in the online version, at doi:<https://doi.org/10.1016/j.jeurceramsoc.2021.04.004>.

References

- [1] B. Cantor, I.T.H. Chang, P. Knight, A.J.B. Vincent, Microstructural development in equiatomic multicomponent alloys, *Mater. Sci. Eng. A* 375–377 (2004) 213–218.
- [2] J.-W. Yeh, S.-J. Lin, T.-S. Chin, J.-Y. Gan, S.-K. Chen, T.-T. Shun, C.-H. Tsau, S.-Y. Chou, Formation of simple crystal structures in Cu-Co-Ni-Cr-Al-Fe-Ti-V alloys with multiprincipal metallic elements, *Metall. Mater. Trans. A* 35 (8) (2004) 2533–2536.
- [3] J.W. Yeh, S.K. Chen, S.J. Lin, J.Y. Gan, T.S. Chin, T.T. Shun, C.H. Tsau, S.Y. Chang, Nanostructured high-entropy alloys with multiple principal elements: novel alloy design concepts and outcomes, *Adv. Eng. Mater.* 6 (5) (2004) 299–303.
- [4] C.M. Rost, E. Sachet, T. Borman, A. Moballeghe, E.C. Dickey, D. Hou, J.L. Jones, S. Curtarolo, J.P. Maria, Entropy-stabilized oxides, *Nat. Commun.* 6 (2015) 8485.
- [5] S. Jiang, T. Hu, J. Gild, N. Zhou, J. Nie, M. Qin, T. Harrington, K. Vecchio, J. Luo, A new class of high-entropy perovskite oxides, *Scr. Mater.* 142 (2018) 116–120.
- [6] J. Gild, M. Samiee, J.L. Braun, T. Harrington, H. Vega, P.E. Hopkins, K. Vecchio, J. Luo, High-entropy fluorite oxides, *J. Eur. Ceram. Soc.* 38 (10) (2018) 3578–3584.
- [7] S. Qiu, M. Li, G. Shao, H. Wang, J. Zhu, W. Liu, B. Fan, H. Xu, H. Lu, Y. Zhou, R. Zhang, (Ca,Sr,Ba)ZrO₃: a promising entropy-stabilized ceramic for titanium alloys smelting, *J. Mater. Sci. Technol.* 65 (2021) 82–88.
- [8] J. Gild, Y. Zhang, T. Harrington, S. Jiang, T. Hu, M.C. Quinn, W.M. Mellor, N. Zhou, K. Vecchio, J. Luo, High-entropy metal diborides: a new class of high-entropy materials and a new type of ultrahigh temperature ceramics, *Sci. Rep.* 6 (2016) 37946.
- [9] J. Gild, K. Kaufmann, K. Vecchio, J. Luo, Reactive flash spark plasma sintering of high-entropy ultrahigh temperature ceramics, *Scr. Mater.* 170 (2019) 106–110.

- [10] M. Qin, Q. Yan, H. Wang, C. Hu, K.S. Vecchio, J. Luo, High-entropy monoborides: towards superhard materials, *Scr. Mater.* 189 (2020) 101–105.
- [11] M. Qin, Q. Yan, Y. Liu, J. Luo, A new class of high-entropy M3B4 borides, *J. Adv. Ceram.* (2020).
- [12] T.J. Harrington, J. Gild, P. Sarker, C. Toher, C.M. Rost, O.F. Dippo, C. McElfresh, K. Kaufmann, E. Marin, L. Borowski, P.E. Hopkins, J. Luo, S. Curtarolo, D. W. Brenner, K.S. Vecchio, Phase stability and mechanical properties of novel high entropy transition metal carbides, *Acta Mater.* 166 (2019) 271–280.
- [13] C.-H. Lai, S.-J. Lin, J.-W. Yeh, S.-Y. Chang, Preparation and characterization of AlCrTaTiZr multi-element nitride coatings, *Surf. Coat. Technol.* 201 (6) (2006) 3275–3280.
- [14] V. Braic, A. Vladescu, M. Balaceanu, C.R. Luculescu, M. Braic, Nanostructured multi-element (TiZrNbHfTa)N and (TiZrNbHfTa)C hard coatings, *Surf. Coat. Technol.* 211 (2012) 117–121.
- [15] T. Jin, X. Sang, R.R. Unocic, R.T. Kinch, X. Liu, J. Hu, H. Liu, S. Dai, Mechanochemical-assisted synthesis of high-entropy metal nitride via a soft urea strategy, *Adv. Mater.* 30 (23) (2018), 1707512.
- [16] Q.-W. Xing, S.-Q. Xia, X.-H. Yan, Y. Zhang, Mechanical properties and thermal stability of (NbTiAlSiZr)_{Nx} high-entropy ceramic films at high temperatures, *J. Mater. Res.* 33 (19) (2018) 3347–3354.
- [17] J. Gild, J. Braun, K. Kaufmann, E. Marin, T. Harrington, P. Hopkins, K. Vecchio, J. Luo, A high-entropy silicide: (Mo_{0.2}Nb_{0.2}Ta_{0.2}Ti_{0.2}W_{0.2})Si₂, *J. Mater.* 5 (3) (2019) 337–343.
- [18] Y. Qin, J.-X. Liu, F. Li, X. Wei, H. Wu, G.-J. Zhang, A high entropy silicide by reactive spark plasma sintering, *J. Adv. Ceram.* 8 (1) (2019) 148–152.
- [19] M. Qin, Q. Yan, H. Wang, K.S. Vecchio, J. Luo, High-entropy rare earth tetraborides, *J. Eur. Ceram. Soc.* 41 (4) (2021) 2968–2973.
- [20] M. Qin, J. Gild, H. Wang, T. Harrington, K.S. Vecchio, J. Luo, Dissolving and stabilizing soft WB₂ and MoB₂ phases into high-entropy borides via boron-metals reactive sintering to attain higher hardness, *J. Eur. Ceram. Soc.* 40 (12) (2020) 4348–4353.
- [21] G. Tallarita, R. Licheri, S. Garroni, R. Orrù, G. Cao, Novel processing route for the fabrication of bulk high-entropy metal diborides, *Scr. Mater.* 158 (2019) 100–104.
- [22] G. Tallarita, R. Licheri, S. Garroni, S. Barbarossa, R. Orrù, G. Cao, High-entropy transition metal diborides by reactive and non-reactive spark plasma sintering: a comparative investigation, *J. Eur. Ceram. Soc.* 40 (4) (2020) 942–952.
- [23] R. Zhang, S. Zhao, J. Ding, Y. Chong, T. Jia, C. Ophus, M. Asta, R.O. Ritchie, A. M. Minor, Short-range order and its impact on the CrCoNi medium-entropy alloy, *Nature* 581 (7808) (2020) 283–287.
- [24] D. Kalish, E.V. Clougherty, K. Kreder, Strength, fracture mode, and thermal stress resistance of HfB₂ and ZrB₂, *J. Am. Ceram. Soc.* 52 (1) (1969) 30–36.
- [25] M.W. Bird, R.P. Aune, A.F. Thomas, P.F. Becher, K.W. White, Temperature-dependent mechanical and long crack behavior of zirconium diboride-silicon carbide composite, *J. Eur. Ceram. Soc.* 32 (12) (2012) 3453–3462.
- [26] W.-W. Wu, Y. Sakka, M. Estili, T.S. Suzuki, T. Nishimura, G.-J. Zhang, Microstructure and high-temperature strength of textured and non-textured ZrB₂ ceramics, *Sci. Technol. Adv. Mater.* 15 (1) (2013), 014202.
- [27] A.G. Evans, A. Rana, High temperature failure mechanisms in ceramics, *Acta Metall Mater* 28 (2) (1980) 129–141.
- [28] D.B. Miracle, O.N. Senkov, A critical review of high entropy alloys and related concepts, *Acta Mater.* 122 (2017) 448–511.
- [29] O.N. Senkov, D.B. Miracle, K.J. Chaput, J.-P. Couzinie, Development and exploration of refractory high entropy alloys—a review, *J. Mater. Res.* 33 (19) (2018) 3092–3128.
- [30] J.Y. He, H. Wang, H.L. Huang, X.D. Xu, M.W. Chen, Y. Wu, X.J. Liu, T.G. Nieh, K. An, Z.P. Lu, A precipitation-hardened high-entropy alloy with outstanding tensile properties, *Acta Mater.* 102 (2016) 187–196.
- [31] S. Failla, P. Galizia, S. Fu, S. Grasso, D. Sciti, Formation of high entropy metal diborides using arc-melting and combinatorial approach to study quinary and quaternary solid solutions, *J. Eur. Ceram. Soc.* 40 (3) (2020) 588–593.
- [32] F.-Z. Dai, Y. Zhou, W. Sun, Segregation of solute atoms (Y, Nb, Ta, Mo and W) in ZrB₂ grain boundaries and their effects on grain boundary strengths: a first-principles investigation, *Acta Mater.* 127 (2017) 312–318.
- [33] H.-B. Ma, J. Zou, J.-T. Zhu, L.-F. Liu, G.-J. Zhang, Segregation of tungsten atoms at ZrB₂ grain boundaries in strong ZrB₂-SiC-WC ceramics, *Scr. Mater.* 157 (2018) 76–80.
- [34] O.N. Senkov, S. Gorse, D.B. Miracle, High temperature strength of refractory complex concentrated alloys, *Acta Mater.* 175 (2019) 394–405.
- [35] O.N. Senkov, S.V. Senkova, C. Woodward, Effect of aluminum on the microstructure and properties of two refractory high-entropy alloys, *Acta Mater.* 68 (2014) 214–228.
- [36] J. Hu, Y.N. Shi, X. Sauvage, G. Sha, K. Lu, Grain boundary stability governs hardening and softening in extremely fine nanograined metals, *Science* 355 (6331) (2017) 1292–1296.
- [37] X.Y. Li, Z.H. Jin, X. Zhou, K. Lu, Constrained minimal-interface structures in polycrystalline copper with extremely fine grains, *Science* 370 (6518) (2020) 831.
- [38] N. Zhou, T. Hu, J. Luo, Grain boundary complexions in multicomponent alloys: challenges and opportunities, *Curr. Opin. Solid State Mater. Sci.* 20 (5) (2016) 268–277.

- [39] N. Zhou, T. Hu, J. Huang, J. Luo, Stabilization of nanocrystalline alloys at high temperatures via utilizing high-entropy grain boundary complexions, *Scr. Mater.* 124 (2016) 160–163.
- [40] Z.P. Lu, H. Wang, M.W. Chen, I. Baker, J.W. Yeh, C.T. Liu, T.G. Nieh, An assessment on the future development of high-entropy alloys: summary from a recent workshop, *Intermetallics* 66 (2015) 67–76.
- [41] S. Praveen, J. Basu, S. Kashyap, R.S. Kottada, Exceptional resistance to grain growth in nanocrystalline CoCrFeNi high entropy alloy at high homologous temperatures, *J. Alloys. Compd.* 662 (2016) 361–367.